viruses

MDPI

Article

SA55 Escape Mutations Are Associated with Increased Sensitivity to Human Plasma Neutralization

Yutong Li [1,2,3,†], Xiao Niu [1,2,4,†], Zhiqiang Li [1], Fanchong Jian [2], Lingling Yu [1], Yuanling Yu [1], Haiyan Sun [1], Jing Wang [1], Fei Shao [1] and Yunlong Cao [1,2,5,*]

[1] Changping Laboratory, Beijing 102206, China; yutongli@stu.pku.edu.cn (Y.L.); pkunx@pku.edu.cn (X.N.); lizq@cpl.ac.cn (Z.L.); yulingling@cpl.ac.cn (L.Y.); yuyuanling@cpl.ac.cn (Y.Y.); a0000120@cpl.ac.cn (H.S.); wangjing@cpl.ac.cn (J.W.); shaofei@cpl.ac.cn (F.S.)
[2] Biomedical Pioneering Innovation Center (BIOPIC), School of Life Sciences, Peking University, Beijing 100871, China; jfc@pku.edu.cn
[3] Academy for Advanced Interdisciplinary Studies, Peking University, Beijing 100871, China
[4] College of Chemistry and Molecular Engineering, Peking University, Beijing 100871, China
[5] Peking–Tsinghua Center for Life Sciences, Peking University, Beijing 100871, China
* Correspondence: yunlongcao@pku.edu.cn
† These authors contributed equally to this work.

Abstract

SA55, isolated from a SARS-CoV-1 convalescent vaccinated against SARS-CoV-2, is a clinically evaluated broadly neutralizing antibody active against SARS-CoV-1 and diverse SARS-CoV-2 variants. Although deep mutational scanning has identified RBD residues 503 and especially 504 as key escape sites for SA55, and repeated Omicron exposures can elicit antibodies recognizing a similar RBD epitope (termed F3), these sites have rarely mutated in nature. Notably, G504 is highly conserved across sarbecoviruses, and both residues 503 and 504 have remained largely unchanged among circulating SARS-CoV-2 lineages, suggesting strong evolutionary constraints. Here, we show that escape from SA55 is constrained because it paradoxically increases viral susceptibility to polyclonal immunity. Using KP.3 pseudoviruses carrying representative escape substitutions, we found that mutations at residues 503 and 504 conferred resistance to SA55 and other F3 antibodies but simultaneously increased sensitivity to antibodies targeting other RBD epitopes and JN.1-convalescent plasma. Moreover, plasma sensitization correlated with increased susceptibility to soluble ACE2-mediated inhibition at selected RBD sites. Together, these findings indicate that SA55 escape mutations may enhance RBD accessibility, thereby increasing viral susceptibility to antibodies targeting other RBD epitopes. This antigenic trade-off likely constrains the emergence of SA55 escape mutations in circulating variants and helps explain its sustained neutralization breadth.

Keywords: SARS-CoV-2; SA55; broadly neutralizing antibody; antibody escape; plasma neutralization; antigenic trade-off

Check for updates

Academic Editor: Ronald N. Harty

Received: 25 October 2026
Revised: 17 November 2026
Accepted: 26 November 2026
Published: 29 November 2026

Copyright: © 2026 by the authors. Licensee MDPI, Basel, Switzerland. This article is an open access article distributed under the terms and conditions of the Creative Commons Attribution (CC BY) license.

1. Introduction

SARS-CoV-2 has undergone extensive antigenic evolution under population-level immune pressure, with successive Omicron lineages acquiring mutations that escape neutralizing antibodies (NAbs) elicited by previous infection or vaccination [1–3]. Since its emergence in late 2021, the Omicron variant has diversified into multiple lineages, including BA.1, BA.2, and BA.5, followed by the recombinant XBB lineage and the distinct BA.2.86

lineage, from which JN.1 and subsequently KP.3 emerged [4–6]. Consequently, many previously potent receptor-binding domain (RBD)-directed monoclonal antibodies (mAbs), including candidates developed for therapeutic use, have lost neutralizing activity against emerging variants [7–10]. Identifying antibodies that retain high potency and breadth during continued viral evolution therefore remains an important goal [11–13]. Among such candidates, SA55 (also designated BD55-5514) was originally isolated from SARS-CoV-1- and SARS-CoV-2-RBD-cross-reactive memory B cells of a SARS-CoV-1 convalescent who subsequently received SARS-CoV-2 vaccination [14]. SA55 recognizes an RBD epitope overlapping the ACE2-binding interface and potently neutralizes SARS-CoV-1, ancestral SARS-CoV-2, and diverse Omicron sublineages [14]. This exceptional breadth has supported its clinical development, including phase I evaluations of intranasal and injectable formulations [15,16]. However, its sustained activity across successive viral waves raises a key question: why have circulating SARS-CoV-2 variants not readily escaped SA55?

Notably, experimental escape from SA55 is achievable. Previous deep mutational scanning (DMS) and in vitro viral selection experiments have identified substitutions at RBD residues 503 and 504 that reduce SA55 neutralization [14]. Initially, the relative rarity of SA55-like broadly neutralizing antibodies in the human population may have limited the selection pressure favoring escape at these sites. However, repeated Omicron exposures have since been shown to elicit antibodies targeting an RBD epitope that overlaps with that recognized by SA55. These antibodies, classified into the F3 epitope group, broadly neutralize multiple Omicron sublineages [17,18]. Although most contemporary Omicron-induced F3 antibodies lack the cross-sarbecovirus breadth of SA55, their DMS escape profiles substantially overlap with that of SA55, particularly at residue 504. Nevertheless, their relative dependence on individual residues differs: SA55 escape is strongly concentrated at residue 504, whereas contemporary F3 antibodies show additional vulnerabilities at residues 403, 405, and 505 [14,17,18].

Evolutionarily, residue 504 is highly conserved across sarbecoviruses, and residue 503 has remained similarly conserved among circulating SARS-CoV-2 lineages [12,14,19], suggesting intrinsic constraints potentially involving ACE2 engagement or other aspects of spike function. Yet, because SA55 escape mutations at these sites can arise under experimental selection and remain compatible with viral replication in vitro [14], their limited prevalence in nature likely reflects selective costs that are not captured by measuring monoclonal antibody escape or in vitro replication alone. Importantly, the effects of RBD mutations on polyclonal antibody recognition can vary substantially across individuals [20], and escape from an individual antibody does not necessarily confer a net selective advantage in a polyclonal immune environment. Indeed, previous full-spike DMS studies have shown that certain substitutions can increase viral sensitivity to human plasma neutralization, potentially by altering spike conformation and RBD accessibility [21,22]. We therefore hypothesized that substitutions at conserved F3-associated sites confer escape from SA55 or other F3 antibodies only at the cost of increased susceptibility to antibodies targeting other RBD epitopes, creating an antigenic trade-off that limits the spread of these substitutions during SARS-CoV-2 evolution.

To test this hypothesis, we characterized the neutralization breadth of SA55, compared its structural recognition and DMS escape profile with those of previously characterized Omicron-induced F3 antibodies, and then investigated representative F3 escape-site substitutions in the KP.3 spike background. JN.1 expanded rapidly in late 2023 and became globally predominant by early 2024, subsequently giving rise to descendant lineages including KP.3 [6,23]. We examined plasma from JN.1-convalescent individuals with prior vaccination and BA.5/BF.7 breakthrough infection, providing a polyclonal immune context shaped by repeated Omicron exposures and evolutionarily relevant to the KP.3 spike background.

Using pseudovirus neutralization assays, we measured the sensitivity of these mutants to F3-, A1-, D3-, and E3-epitope mAbs, plasma from JN.1-convalescent individuals, and soluble ACE2-mediated inhibition. We found that escape-associated substitutions—most consistently at residue 504—reduced sensitivity to SA55 but simultaneously increased susceptibility to other RBD-directed antibodies and JN.1-convalescent plasma neutralization. Furthermore, this plasma sensitization was associated with increased sensitivity to soluble ACE2-mediated inhibition, consistent with enhanced RBD accessibility and potential shifts toward RBD-up/down conformational dynamics. These findings reveal an antigenic trade-off that constrains the net selective advantage of SA55 escape mutations in polyclonal immune environments, helping to explain why such substitutions have not become prevalent in circulating SARS-CoV-2 lineages.

2. Materials and Methods

2.1. Participants and Plasma Isolation

Blood samples were collected from nine individuals who had experienced an initial Omicron BA.5/BF.7 breakthrough infection followed by JN.1 reinfection. Participants ranged from 32 to 60 years of age (mean ± s.d., 46.8 ± 11.1 years) and included six females and three males. All participants had received two or three doses of inactivated SARS-CoV-2 vaccines prior to their first breakthrough infection. The BA.5/BF.7 breakthrough infections occurred predominantly in late 2022, whereas the subsequent JN.1 reinfections occurred between February and March 2024. Blood samples were collected 19–52 days after JN.1 reinfection, with a mean interval of 31.3 ± 10.6 days (mean ± s.d.). The study was conducted under protocols approved by the Ethics Committee of Tianjin First Central Hospital (Approval No. 2022N151KY-02; approval date: 4 February 2024). All participants provided written informed consent for the collection, storage, and research use of their blood samples and for the publication of the resulting data. Detailed demographic and clinical information for the human donors involved in this study is provided in Table S1.

Venous whole blood (20 mL per participant) was collected into EDTA-containing anticoagulant tubes and maintained at room temperature before processing. Whole blood was diluted 1:1 with phosphate-buffered saline (PBS; Gibco, C10010500BT, Suzhou, China) supplemented with 2% fetal bovine serum (FBS; Cytiva, SH30406.05, Tauranga, New Zealand). SepMate™-50 (RUO) tubes (STEMCELL Technologies, 86450, Vancouver, BC, Canada) were preloaded with 15 mL Ficoll-Paque PLUS density-gradient medium (Cytiva, 17-1440-03, Uppsala, Sweden), and the diluted blood was transferred into the tubes. Samples were centrifuged at 1200× *g* for 10 min at room temperature using a swing-out rotor. Following centrifugation, the clear, pale-yellow upper plasma-containing layer was carefully transferred into a fresh 1.5-mL or 15-mL tube without disturbing the underlying cellular layer. Approximately 20 mL of the plasma-containing fraction was recovered from each donor. Samples were stored at −80 °C until use. Prior to neutralization assays, plasma samples were heat-inactivated at 56 °C for 30 min.

2.2. Pseudovirus Preparation

Spike-pseudotyped viruses were generated using a vesicular stomatitis virus (VSV)-based packaging system as described previously [18,24]. Specifically, we constructed pseudoviruses bearing the spike proteins of SARS-CoV-1, other sarbecoviruses (WIV1, RaTG13, pangolin-CoV-GD, and Khosta-2), representative SARS-CoV-2 variants (Figure 1c), and a panel of KP.3 single-site mutants carrying substitutions at residues 404, 440, 503, 504, and 505. Codon-optimized spike genes encoding the indicated spike proteins were cloned into the pcDNA3.1 vector. Subsequently, 293T cells (ATCC, CRL-3216, Manassas, VA, USA) were transfected with the corresponding spike-expression plasmids and infected

with G*ΔG-VSV virus (Kerafast, EH1020-PM, Boston, MA, USA). After 48 h of incubation, pseudovirus-containing supernatants were harvested, filtered through a 0.45-μm polyethersulfone membrane filter, aliquoted, and stored at −80 °C until use.

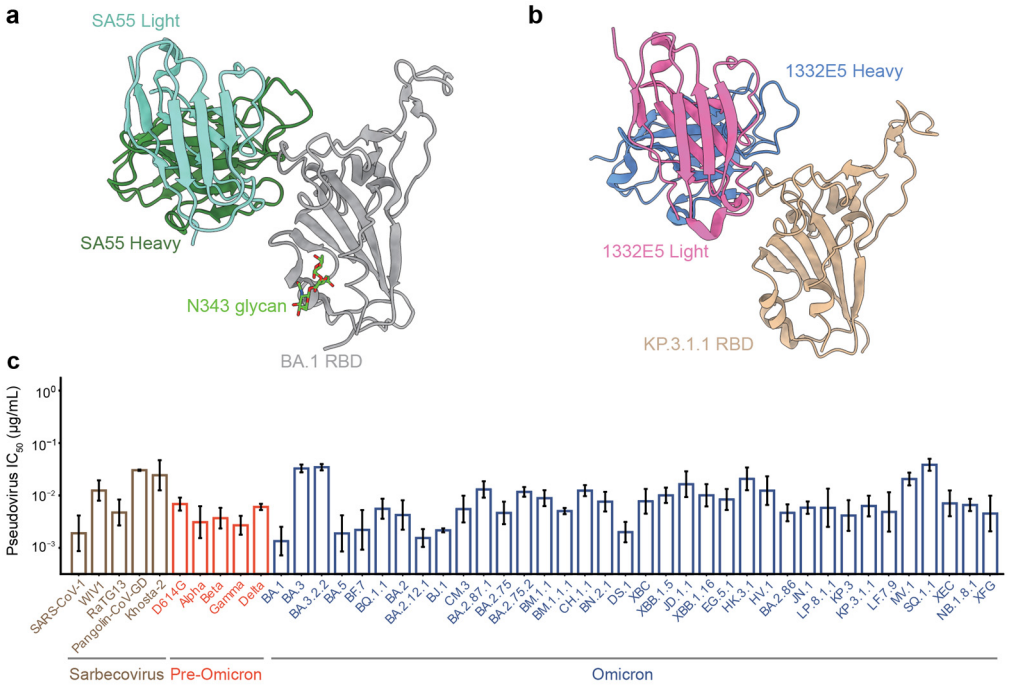


Figure 1. Structure and neutralization profiles of SA55. (**a**) Cartoon representation of the cryo-EM structure of SA55 Fab bound to the SARS-CoV-2 BA.1 RBD (PDB: 7Y0W) [14]. The SA55 heavy and light chains are colored in dark green and cyan, respectively, and the BA.1 RBD is colored in gray; the N343-linked glycan is shown as sticks. (**b**) Cartoon representation of the cryo-EM structure of 1332E5 Fab bound to the SARS-CoV-2 KP.3.1.1 RBD (PDB: 11IT) [25]. The 1332E5 heavy and light chains are colored in blue and magenta, respectively, and the KP.3.1.1 RBD is colored in tan. (**c**) Neutralization activity of SA55 against diverse sarbecoviruses and SARS-CoV-2 variants. Bars represent geometric mean half-maximal inhibitory concentrations (IC_{50}, μg/mL), with error bars indicating geometric standard deviations (GSDs). Brown, red, and blue bar outlines represent sarbecoviruses other than SARS-CoV-2, pre-Omicron SARS-CoV-2 variants, and Omicron SARS-CoV-2 variants, respectively. Each pseudovirus was tested in at least two independent experiments. Some neutralization data were previously reported.

2.3. Pseudovirus Neutralization Assay

Pseudovirus neutralization assays were conducted using Huh-7 cells (JCRB Cell Bank, 0403, Ibaraki, Osaka, Japan). Serially diluted mAbs, plasma samples, or soluble ACE2 were mixed with pseudoviruses in 96-well plates and incubated for 1 h at 37 °C with 5% CO_2. Detached Huh-7 cells were then added to each well and cultured for an additional 24 h. After incubation, the supernatant was partially aspirated, leaving 50 μL in each well, and luciferase activity was measured using Bright-Lite Plus Luciferase Assay Substrate reconstituted with Bright-Lite Plus Luciferase Assay Buffer (Vazyme, DD1209-03-AB, Nanjing, China). Following a 2-min incubation in the dark, luminescence was quantified using a EnSight Multimode Plate Reader (PerkinElmer, HH3400, Waltham, MA, USA). The 50% neutralization titer (NT_{50}) values for plasma samples and half-maximal inhibitory concentration (IC_{50}) values for mAbs or soluble ACE2 were determined by fitting dose–response curves using two- or three-parameter logistic regression models implemented in Python 3.10.11 with SciPy 1.13.0 and NumPy 1.26.4, as appropriate.

2.4. DMS Library Construction

Yeast surface display enables conformationally intact RBD variants to be screened for antibody binding in a high-throughput manner, making it well suited for comprehensive mapping of antibody-escape mutations [19,26]. Replicate DMS libraries of the SARS-CoV-2 JN.1 and XBB.1.5 RBDs, covering residues N331–T531 according to Wuhan-Hu-1 reference numbering, were generated as described previously [7,19]. Computationally designed NNS primer pairs were used for site-directed mutagenesis PCR to introduce all possible single amino-acid substitutions across the RBD region. The mutagenized RBD fragments were subsequently tagged with unique 26-nucleotide (N26) barcodes by PCR and cloned into a yeast surface display vector. To amplify the barcoded libraries, the resulting plasmids were transformed into electrocompetent *Escherichia coli* DH10B-Plus cells (Shanghai Maokang Biotechnology, MF2393-1000UL, Shanghai, China). Variant–barcode associations were resolved by PacBio long-read sequencing of libraries prepared from the amplified plasmid pools. The validated plasmid libraries were then transformed into the EBY100 strain of *Saccharomyces cerevisiae* (ATCC, MYA-4941, Manassas, VA, USA). Transformed yeast cells were selected on SD-CAA agar plates, expanded in SD-CAA liquid medium, flash-frozen in liquid nitrogen, and stored at −80 °C until use.

2.5. MACS-Based Antibody Mutation Escape Profiling

High-throughput mutational escape profiling of mAbs was performed using magnetic-activated cell sorting (MACS), following a previously described protocol [7,9,27]. Prior to antibody selection, the XBB.1.5 and JN.1 RBD DMS libraries were enriched for properly folded, ACE2-binding variants. Briefly, misfolded or non-functional RBD variants were depleted by incubating the induced yeast libraries with biotinylated ACE2 (Sino Biological, 10108-H08H-B, Beijing, China) and capturing ACE2-bound cells using biotin binder beads (Thermo Fisher Scientific, 11533D, Waltham, MA, USA). After washing with PBSA, the bead-captured RBD-expressing yeast cells were recovered, expanded in SD-CAA medium, and preserved as frozen aliquots at −80 °C.

For antibody escape profiling, the ACE2-enriched yeast libraries were thawed and cultured overnight in SD-CAA with shaking. The cultures were then back-diluted into SG-CAA medium to induce RBD surface expression. For each mAb, two consecutive rounds of negative selection were carried out to deplete antibody-binding yeast variants from the library. The remaining antibody-escaping population was subsequently subjected to c-Myc-tag-based positive selection using anti-c-Myc magnetic beads (Thermo Fisher Scientific, 88843, Rockford, IL, USA) to recover only those yeast cells that retained productive RBD surface expression after antibody selection.

The final selected yeast population was washed and expanded overnight in SD-CAA medium. Plasmids were extracted using a 96-well yeast plasmid extraction kit (Coolaber, PE053, Beijing, China), and the N26 barcode region was amplified by PCR using the extracted plasmids as templates. The resulting PCR amplicons were purified with 1× AMPure XP beads (Beckman Coulter Life Sciences, A63882, Indianapolis, IN, USA) and subjected to high-throughput single-end sequencing.

2.6. Antibody DMS Data Analysis

Raw sequencing data from antibody DMS experiments were processed as described previously [7,9,27]. Barcode sequences recovered from both the antibody-selected and reference libraries were mapped to the barcode–variant dictionary generated from PacBio long-read sequencing of the JN.1 or XBB.1.5 RBD DMS libraries using alignparse v0.6.2 and dms_variants v1.4.3. Ambiguous barcodes were removed during the merging of replicate yeast libraries, and barcodes detected five or fewer times in the reference library were excluded

from downstream analysis. For each RBD variant X present in both the antibody-selected and reference libraries, the escape score was defined as: $F \times (n_{X,ab}/N_{ab})/(n_{X,ref}/N_{ref})$, where F is a scaling factor that normalizes the escape scores to the 0–1 range; $n_{X,ab}$ and $n_{X,ref}$ denote the numbers of barcodes assigned to variant X in the antibody-selected and reference libraries, respectively; and N_{ab} and N_{ref} denote the total barcode counts in the corresponding samples. When multiple replicate DMS libraries were analyzed for the same antibody, the final escape score for each mutation was calculated as the average across replicates and used for downstream visualization and comparison.

2.7. Reanalysis of Previously Published F3 Antibody DMS Data

Processed mutation-level DMS escape scores for F3-epitope antibodies were obtained from the dataset accompanying Jian et al. [18], which is publicly available through Zenodo (https://doi.org/10.5281/zenodo.13893217) [28]. We selected a subset of 19 F3-epitope mAbs with available DMS escape data in both the XBB.1.5 and JN.1 RBD backgrounds. For each RBD background, mutation-level escape scores were averaged across these selected antibodies and visualized as sequence-logo plots.

2.8. Integration of RBD–ACE2 Binding Affinity DMS Data

Mutation-level RBD–ACE2 binding affinity DMS data were obtained from Taylor and Starr [29,30]. These datasets measured the effects of single amino-acid substitutions on ACE2-binding affinity using yeast-displayed RBD libraries and fluorescence-activated cell sorting (FACS) across an ACE2 concentration gradient. For the antibody escape maps in Figure 2c,d, we used the XBB.1.5 RBD dataset to color the XBB.1.5 escape profiles and the KP.3.1.1 RBD dataset as a closely related reference for the JN.1 escape profiles. The effect of each substitution on ACE2-binding affinity was represented by the reported delta_bind value, defined as the difference in $-\log_{10}(KD)$ between the mutant and its corresponding parental RBD.

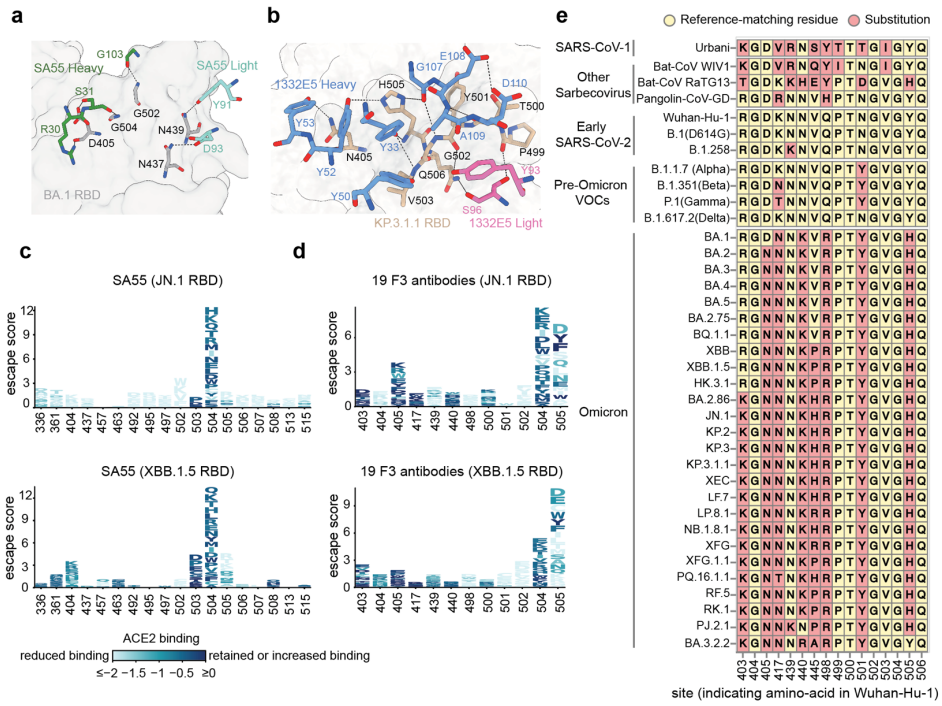


Figure 2. Distinct residue-level recognition and mutational escape profiles of SA55 and Omicron-induced F3 antibodies. (**a**,**b**) Close-up views of the antibody–RBD interfaces for SA55 bound to the BA.1 RBD ((**a**); PDB: 7Y0W) [14] and 1332E5 bound to the KP.3.1.1 RBD ((**b**); PDB: 11IT) [25].

Antibody heavy and light chains and RBDs are colored as in Figure 1a,b. Selected interfacial residues are shown as sticks, with dashed lines indicating hydrogen bonds. (**c**) Average DMS mutation escape scores across two independent replicates for SA55 in the JN.1 (top) and XBB.1.5 (bottom) RBD backgrounds. (**d**) Average DMS mutation escape scores for F3-epitope mAbs in the JN.1 (top) and XBB.1.5 (bottom) RBD backgrounds ($n = 19$). F3 antibody DMS data were reanalyzed from the previously published dataset of Jian et al. [18]. In (**c**,**d**), the height of each letter represents the escape score of the indicated amino-acid substitution. Letters are colored according to previously reported effects on RBD–ACE2 binding affinity, measured by yeast-display DMS in the KP.3.1.1 [30] and XBB.1.5 [29] RBD backgrounds for the JN.1 and XBB.1.5 escape maps, respectively. Color values are capped at −2 and 0. (**e**) Amino-acid identities at selected RBD positions within and adjacent to the SA55/F3 epitope across representative SARS-CoV-2 lineages and other sarbecoviruses. Sequences are grouped into early SARS-CoV-2 lineages, pre-Omicron variants of concern (VOCs), Omicron lineages, SARS-CoV-1, and other sarbecoviruses. Wuhan-Hu-1 was used as the reference sequence, with reference-matching residues highlighted in yellow and substitutions highlighted in pale red. Residue numbering follows the Wuhan-Hu-1 spike sequence.

2.9. Statistical Analysis

Statistical analyses were performed using Python 3.14.7 and R 4.4.2. Individual KP.3 mutants were compared with parental KP.3 using two-sided paired *t*-tests on $\log_{10}$-transformed NT_{50} or IC_{50} values in R 4.4.2 (stats::t.test). Site-specific comparisons of mutation-level $\log_2$ fold-change phenotypes were performed using two-sided Wilcoxon signed-rank tests in SciPy 1.18.1. Pearson correlation coefficients were calculated using NumPy 2.5.2. Hierarchical clustering of plasma neutralization profiles was performed in R 4.4.2 using a distance of 1 − Pearson correlation and average linkage. Statistical significance thresholds are specified in the corresponding figure legends.

3. Results

3.1. SA55 Exhibits Broad Neutralization Across Sarbecoviruses and SARS-CoV-2 Variants

To understand the structural basis of F3-epitope recognition, we first compared the previously reported cryo-EM structures of SA55 bound to the BA.1 RBD and the Omicron-induced F3 antibody 1332E5 bound to the KP.3.1.1 RBD (Figure 1a,b) [14,25]. Both antibodies recognize a similar RBD surface encompassing residues 498–506, which forms part of the ACE2-binding interface.

We then evaluated the neutralization breadth of SA55 against a panel of sarbecovirus and SARS-CoV-2 pseudoviruses (Figure 1c, Table S2). SA55 potently neutralized all tested sarbecoviruses, including SARS-CoV-1, WIV1, RaTG13, pangolin-CoV-GD, and Khosta-2. It also maintained potent neutralizing activity against ancestral and pre-Omicron SARS-CoV-2 strains, as well as diverse Omicron lineages spanning BA.1, BA.2, BA.3, BA.5, XBB, BA.2.86/JN.1, and their descendants, demonstrating its exceptional neutralization breadth. In contrast, previous studies have shown that contemporary Omicron-induced F3 antibodies generally exhibit broad neutralization across Omicron sublineages but limited activity against SARS-CoV-1, ancestral SARS-CoV-2 and the highly divergent BA.3.2.2 lineage [17,18,25,31]. Thus, despite recognizing a similar RBD region, SA55 and Omicron-induced F3 antibodies exhibit distinct neutralization breadth.

3.2. SA55 Escape Maps Identify a Focused Region of Vulnerability

To elucidate the molecular basis underlying these differences in neutralization breadth, we compared the residue-level structural interactions and DMS escape profiles of SA55 and Omicron-induced F3 antibodies. In the previously reported SA55–BA.1 RBD structure, SA55 forms key contacts with several RBD residues, including D405, N437, N439, G502, and G504 (Figure 2a) [14]. By comparison, the structure of the Omicron-induced F3

antibody 1332E5 bound to the KP.3.1.1 RBD reveals extensive interactions across residues 498–506—particularly V503 and H505—as well as N405 (Figure 2b) [25]. These structural comparisons indicate that although SA55 and 1332E5 recognize overlapping RBD surfaces, they rely on distinct residue-level interactions.

Consistent with these structural differences, the two antibody groups exhibited distinct mutational escape profiles. DMS of SA55 in both the JN.1 and XBB.1.5 RBD backgrounds revealed a highly focused escape hotspot at residue 504, with only minor contributions from neighboring residues (Figure 2c). In contrast, the mean escape profiles of 19 previously characterized F3 antibodies overlapped with that of SA55 at residue 504 but were dominated by stronger escape signals at residue 505, accompanied by additional vulnerabilities at residues 403 and 405 (Figure 2d) [18]. To assess the effects of these escape-associated substitutions on receptor binding, we integrated published RBD–ACE2 affinity DMS data from the XBB.1.5 and KP.3.1.1 backgrounds [29,30]. Notably, many substitutions at residue 504 retained substantial ACE2-binding affinity, suggesting that escape at this site does not necessarily entail a severe loss of intrinsic receptor-binding function (Figure 2c,d).

To assess how these divergent escape dependencies relate to viral evolution, we next examined the evolutionary conservation of these escape-associated residues across representative SARS-CoV-2 lineages, SARS-CoV-1, and related bat and pangolin sarbecoviruses (Figure 2e). Residue 505 exhibited notable variation during SARS-CoV-2 evolution: the ancestral Y505 was replaced by H505 upon the emergence of Omicron, whereas the highly divergent BA.3.2.2 lineage carries an H505Y reversion. This variability at position 505 likely explains the reduced neutralization sensitivity of ancestral SARS-CoV-2 and BA.3.2.2 to contemporary Omicron-induced F3 antibodies. In striking contrast, G504 remained strictly conserved across all examined sequences, including SARS-CoV-1, related sarbecoviruses, and diverse SARS-CoV-2 lineages. Similarly, residue 503 was conserved across all examined SARS-CoV-2 lineages, although amino-acid variation was observed among other sarbecoviruses. The remarkable conservation of G504, despite its experimentally demonstrated capacity to mediate antibody escape, suggests that substitutions at this position face strong evolutionary constraints [12,19]. Notably, a previous full-spike DMS study indicated that G504 substitutions can increase viral sensitivity to human serum neutralization [22]. Prompted by this observation, we investigated whether SA55 escape at this conserved site is accompanied by increased susceptibility to antibodies targeting other RBD epitopes and to polyclonal plasma.

3.3. SA55 Escape at Residue 504 Coincides with Increased Plasma Neutralization Sensitivity

To determine whether mutations at F3-associated escape sites affect susceptibility to polyclonal plasma neutralization, we generated KP.3 pseudoviruses carrying representative single amino-acid substitutions at RBD residues 404, 440, 503, 504, and 505, and assessed their sensitivity to F3-directed antibodies, plasma from nine JN.1-convalescent individuals, and soluble ACE2 (Figure 3a and Table S3). Consistent with our DMS findings, SA55 escape was predominantly driven by substitutions at residue 504, whereas VYD222 [32,33], another F3-epitope antibody, exhibited broader escape vulnerabilities across multiple sites (Figures 3a and S1).

Notably, substitutions at residues 503 and 504 generally increased plasma neutralization sensitivity across the donor cohort, demonstrating a robust sensitizing phenotype despite inter-individual differences in neutralization profiles (Figure 3a). Relative to parental KP.3, substitutions at residues 503 and 504 increased the geometric mean plasma neutralization titers by 2.1–9.7-fold and 2.2–12-fold, respectively (Figure S2). Similar plasma-sensitizing effects were observed for substitutions at residues 404 and 505. In contrast, substitutions at residue 440 produced more heterogeneous responses, yielding both sensi-

tizing and escape phenotypes across different amino-acid substitutions and plasma donors (Figures 3a and S2).

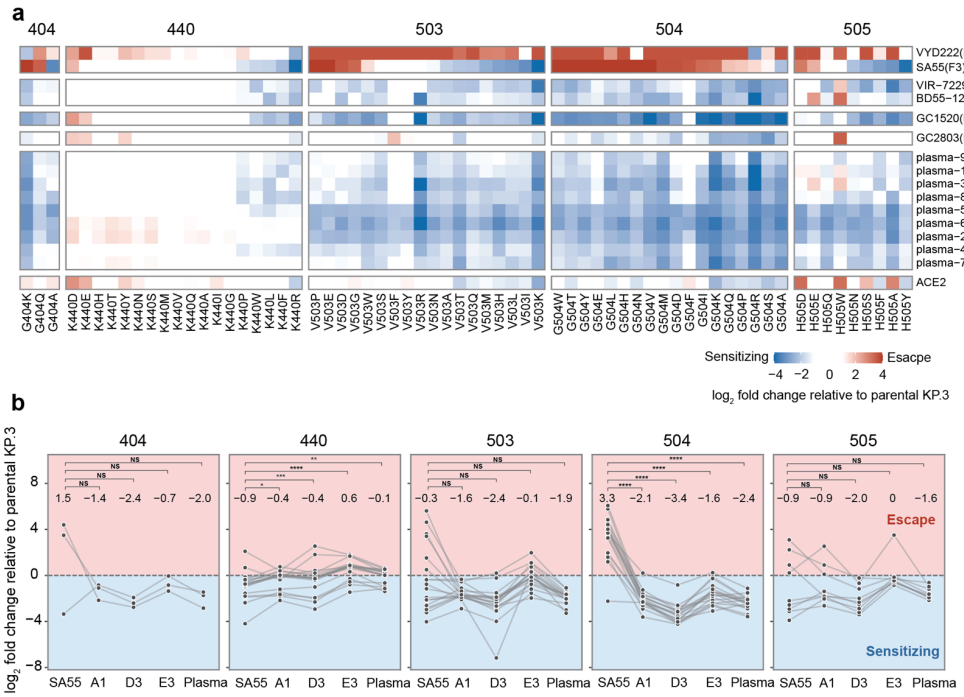


Figure 3. Effects of representative F3 escape-site mutations on sensitivity to mAbs, human plasma, and soluble ACE2. (**a**) Heatmap showing the phenotypic effects of single amino-acid substitutions at RBD residues 404, 440, 503, 504, and 505 in the KP.3 spike background. Mutants were grouped by residue and ordered within each group by decreasing SA55 escape score. Rows represent F3 (VYD222 and SA55), A1 (VIR-7229 and BD55-1205), D3 (GC1520), and E3 (GC2803) mAbs, plasma from nine JN.1-convalescent individuals, and soluble ACE2. Plasma samples were ordered by hierarchical clustering using Pearson correlation distance and average linkage. Escape scores were calculated as $\log_2[IC_{50}(\text{mutant})/IC_{50}(\text{KP.3})]$ for mAbs and soluble ACE2, and $\log_2[NT_{50}(\text{KP.3})/NT_{50}(\text{mutant})]$ for each plasma sample. ACE2 scores were based on geometric mean IC_{50} values from three replicates. Positive and negative values indicate escape and sensitization, respectively. A diverging color scale was used, with values between −1 and +1 displayed in white. Color values are capped at ±4. (**b**) Site-specific paired comparisons of SA55 escape scores with the corresponding phenotypes of A1, D3, and E3 antibodies and JN.1-convalescent plasma for the same single amino-acid substitutions. Each black dot represents the $\log_2$ fold change for an individual KP.3 single-mutant pseudovirus in the corresponding group, with gray lines connecting values for the same mutant across groups. The horizontal dashed line at zero indicates no change relative to parental KP.3. Numbers indicate the arithmetic mean $\log_2$ fold change for each group. Pairwise comparisons of A1, D3, E3, and plasma versus SA55 were performed using two-sided Wilcoxon signed-rank tests, with the substituted amino acid as the pairing unit and Holm correction applied within each site. NS, not significant; * $p < 0.05$; ** $p < 0.01$; *** $p < 0.001$; **** $p < 0.0001$.

Residue 504 was of particular interest because it represents the dominant SA55 escape hotspot identified by DMS. Strikingly, while all tested G504 substitutions except G504A reduced sensitivity to SA55, every tested G504 substitution simultaneously increased sensitivity to JN.1-convalescent plasma (Figure 3a). At the site level, the mean $\log_2$ fold change relative to parental KP.3 was +3.3 for SA55 escape but −2.4 for plasma neutralization (representing net sensitization), highlighting diametrically opposite effects on SA55 and polyclonal plasma activity (Figure 3b). Together, these findings establish G504 substitutions as a prominent example of monoclonal antibody escape accompanied by broadly consistent sensitization to human polyclonal plasma.

3.4. Enhanced Sensitivity of G504 Mutants to Other RBD-Directed Antibodies

To determine whether this heightened plasma sensitivity was driven by enhanced susceptibility to non-F3 neutralizing antibodies, we evaluated the neutralization of G504 mutants by mAbs targeting other major RBD epitopes, including the A1 antibodies VIR-7229 [34] and BD55-1205 [35], the D3 antibody GC1520 [17], and the E3 antibody GC2803 [18]. In stark contrast to their resistance to SA55, most G504 mutants showed markedly increased sensitivity to A1-, D3-, and E3-directed antibodies (Figures 3a,b and S1). Specifically, at residue 504, the mean $\log_2$ IC_{50} fold changes relative to parental KP.3 were −2.1 for A1 antibodies, −3.4 for the D3 antibody GC1520, and −1.6 for the E3 antibody GC2803, compared with +3.3 for SA55 (Figure 3b). These results demonstrate that substitutions conferring resistance to SA55 simultaneously sensitize the virus to antibodies targeting distinct RBD epitopes.

3.5. Plasma Neutralization Sensitivity Correlates with Soluble ACE2 Sensitivity at Selected RBD Sites

To investigate the mechanistic basis underlying this increased neutralization sensitivity, we examined the relationship between polyclonal plasma escape and soluble ACE2-mediated inhibition across the KP.3 single-mutant panel (Figures 4 and S3). The two phenotypes showed positive correlations at residues 440, 503, and 504 (Pearson $r = 0.75$, 0.61, and 0.62, respectively), although substitutions at residue 440 spanned both escape and sensitizing regimes. Because only three substitutions were tested at residue 404, no correlation coefficient was reported for this site. Notably, at residue 504, nearly all substitutions that conferred SA55 escape concurrently increased sensitivity to both JN.1-convalescent plasma and soluble ACE2-mediated inhibition. A similar co-sensitization trend was observed at residue 503, although the effects of mutations at this site on SA55 neutralization were more variable. Collectively, these findings reveal site-dependent associations between plasma and soluble ACE2 sensitivity, with residue 504 exhibiting the most consistent coupling between SA55 escape and concurrent sensitization to both polyclonal plasma and soluble ACE2.

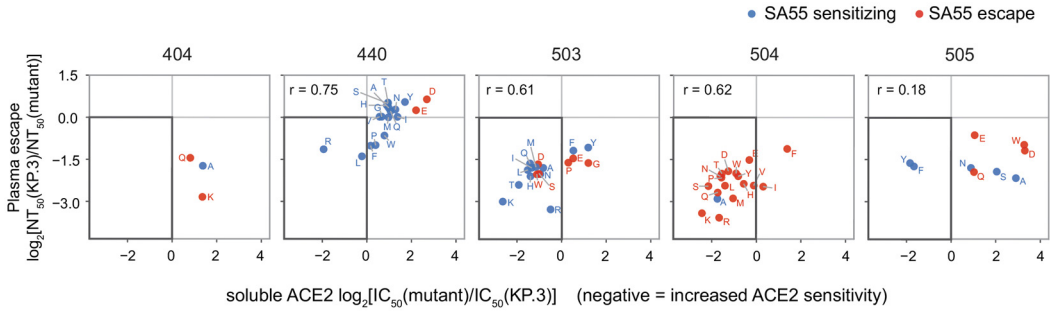


Figure 4. Relationship between soluble ACE2 sensitivity and human plasma escape for single amino-acid substitutions at residues 404, 440, 503, 504, and 505. Each point represents a KP.3 single-mutant pseudovirus and is labeled by the substituted amino acid. Plasma escape and soluble ACE2 phenotypes are defined as in Figure 3. Points are colored according to their SA55 neutralization phenotypes, defined as $\log_2[IC_{50}(\text{mutant})/IC_{50}(\text{KP.3})]$. Red indicates SA55 escape mutations ($\log_2$ fold change > 0), whereas blue indicates SA55 sensitizing mutations ($\log_2$ fold change < 0). Pearson correlation coefficients (r) are shown for residues 440, 503, 504, and 505. No correlation coefficient is reported for residue 404 because only three substitutions were tested at this site.

4. Discussion

SA55 has maintained potent neutralizing activity across antigenically divergent SARS-CoV-2 variants despite the existence of experimentally accessible escape mutations. Our findings identify an antigenic trade-off that helps explain this evolutionary durability. In the

KP.3 background examined here, most G504 substitutions substantially reduced sensitivity to SA55 but simultaneously heightened susceptibility to JN.1-convalescent plasma and monoclonal antibodies targeting other RBD epitopes. Notably, this plasma-sensitizing effect was broadly consistent across all nine convalescent donors. These observations indicate that mutations conferring escape from SA55 concurrently increase viral vulnerability to the broader polyclonal antibody repertoire, thereby limiting their net selective advantage during SARS-CoV-2 evolution.

Although SA55 and contemporary Omicron-induced F3 antibodies recognize overlapping RBD surfaces, they exhibit distinct neutralization breadth and mutational escape profiles. SA55 retains potent neutralizing activity against SARS-CoV-1, ancestral SARS-CoV-2, and diverse Omicron sublineages, including recently emerging variants [10,36–39]. In contrast, contemporary Omicron-induced F3 antibodies are largely restricted to cross-Omicron neutralization and show minimal activity against ancestral strains [14,17,18,25]. The highly divergent BA.3.2.2 lineage illustrates how these distinct residue dependencies shape antibody escape during natural viral evolution. BA.3.2.2 carries numerous spike mutations, including an H505Y reversion to the ancestral residue, which may drive escape from Omicron-induced F3 antibodies that heavily rely on H505 [25,31,40]. In contrast, SA55 retains potent neutralizing activity against BA.3.2.2, reflecting its primary reliance on the strictly conserved residue G504 rather than residue 505 [41]. Dadonaite et al. also identified SA55 neutralization escape effects at residues 440 and 445 in the KP.3.1.1 background [21]. Our KP.3 pseudovirus experiments similarly detected reduced sensitivity to SA55 for K440D and K440E, whereas the other tested K440 substitutions increased sensitivity, indicating substitution-dependent effects. At residue 445, SA55 retained potent neutralizing activity against multiple naturally occurring variant spikes carrying substitutions at this position. Together with the absence of a prominent escape signal at residue 445 in our RBD-based DMS, these observations did not suggest that this site was a major determinant of SA55 escape in the backgrounds examined here.

The scarcity of substitutions at residues 503 and 504 in circulating lineages is particularly striking given their capacity to mediate monoclonal antibody escape. While the rarity of SA55-like antibodies in the general population may have historically limited direct selection pressure on these sites [14], repeated Omicron exposures are now known to elicit abundant F3-directed antibody responses with overlapping escape vulnerabilities [17,18]. The continued conservation of residues 503 and 504—despite the fact that escape substitutions can arise and support viral replication under experimental conditions [12,14]—therefore implies the presence of additional evolutionary constraints. Our findings reveal one such constraint: the antigenic benefit of escaping F3-directed antibodies is counterbalanced by heightened susceptibility to other components of polyclonal immunity. In particular, G504 substitutions markedly enhanced sensitivity to A1- and D3-directed antibodies, which constitute major neutralizing components against recent Omicron variants [17,18,42]. Consequently, the net fitness effect of these substitutions in a polyclonal immune environment differs fundamentally from their effect against isolated F3 antibodies. At the same time, the evolutionary trajectory of such antigenic trade-offs may depend on the broader spike genetic context. Previous studies have demonstrated that epistatic interactions among RBD mutations can buffer receptor-binding defects or enhance ACE2 affinity while facilitating antibody evasion [43,44]. Whether future epistatic substitutions could similarly mitigate the antigenic costs associated with mutations at residues 503 and 504 remains an open question.

The positive correlation between plasma sensitization and soluble ACE2 sensitivity provides a potential clue to the mechanism underlying this antigenic trade-off. Consistent with our observations, a previous full-spike DMS study in the XBB.1.5 background found

that G504 substitutions increased viral sensitivity to human serum neutralization, with serum escape inversely correlated with ACE2 binding at this site [21,22]. Subsequent profiling in the KP.3.1.1 background revealed more variable effects at residues 504 and 505 across serum samples, with some post-exposure sera showing modest escape or minimal sensitization [21]. Considered alongside our KP.3 data, these findings suggest that the magnitude of G504-associated plasma sensitization is modulated by both the spike genetic background and host immune exposure history. In our study, the concurrent increase in sensitivity to soluble ACE2-mediated inhibition and neutralization by plasma and non-F3 antibodies suggests that G504 substitutions may affect RBD accessibility. Although altered RBD-up/down conformational dynamics could provide one possible explanation for these observations, the structural basis of this phenotype remains to be determined.

More broadly, the evolutionary impact of this antigenic trade-off likely depends on the immunodominance hierarchy of population-level antibody immunity. Previous studies have shown that ancestral SARS-CoV-2 immune imprinting and repeated Omicron exposures progressively reshape the relative abundance of distinct RBD-directed antibody classes [17,18]. Specifically, A1-epitope antibodies—frequently encoded by *IGHV3-53*/*IGHV3-66*—dominate ancestral-strain-imprinted neutralizing responses, whereas repeated Omicron exposures increasingly expand Omicron-specific F3-epitope responses [17,18,31]. Within this framework, our finding that G504 substitutions markedly sensitize the virus to A1-directed antibodies suggests that such mutations incur an especially steep antigenic penalty in hosts whose neutralizing repertoires remain rich in A1-like antibodies. It should be noted, however, that our plasma cohort comprised individuals primed with inactivated vaccines prior to Omicron breakthrough infections. Because primary vaccination platforms can differentially shape memory B cell recall and neutralizing specificity against SARS-CoV-2 variants [45,46], further studies will be needed to determine whether G504-associated plasma sensitization is similarly pronounced in populations with distinct vaccination and infection histories.

From a translational perspective, the exceptional neutralization breadth and evolutionary durability of SA55 against SARS-CoV-1 and diverse SARS-CoV-2 variants underscore its value for antibody-based prophylaxis and therapy [14–16]. Moreover, rational antibody engineering can further fortify its resilience against potential escape variants. Previous work has shown that converting SARS-CoV-2-neutralizing IgG antibodies into dimeric or secretory IgA formats markedly enhances neutralization potency against Omicron variants [47], and engineering SA55 into polymeric IgA1 formats was recently shown to restore or enhance neutralization against several escape substitutions at residues 503 and 504 [48]. Beyond passive immunization, our findings also inform vaccine design strategies aimed at eliciting similarly durable neutralizing responses. Specifically, immunogens engineered to focus B cell responses onto the conserved structural determinants surrounding residues 503 and 504—potentially deployed via heterologous sequential immunization—could help elicit SA55-like antibodies capable of broad protection against diverse sarbecoviruses [49–53].

Several limitations of this study should be considered. First, our site-directed mutational analyses were conducted in the KP.3 spike background; because epistatic interactions can alter the phenotypic effects of individual RBD substitutions across divergent viral lineages [29,44,54], these trade-offs should be evaluated in additional emerging variants. Second, although the concurrent sensitization to soluble ACE2 and non-F3 antibodies is consistent with increased RBD exposure, we did not directly assess whether G504 substitutions affect spike structural stability or the equilibrium between RBD-up and RBD-down spike conformations [55,56]. Third, our polyclonal neutralization assays relied on plasma from a modest-sized cohort of JN.1-convalescent donors; given that infection history, vaccination regimens, and immune imprinting shape neutralization immunodominance, the net poly-

clonal effect of SA55 escape mutations may vary across cohorts [18,21]. Finally, VSV-based pseudovirus assays capture spike-mediated entry and neutralization but do not directly measure authentic viral replication fitness, host-to-host transmission, or population-level selection dynamics [22,57].

5. Conclusions

In summary, we demonstrate that in the KP.3 spike background, most tested substitutions at the conserved G504 residue confer resistance to SA55 at the expense of heightened susceptibility to JN.1-convalescent plasma and antibodies targeting distinct RBD epitopes. This polyclonal sensitization correlates with increased sensitivity to soluble ACE2-mediated inhibition, pointing to enhanced RBD accessibility as a likely underlying mechanism. Together, these findings reveal that escaping SA55 imposes a substantial antigenic cost in polyclonal immune environments, thereby constraining the emergence of such mutations in circulating SARS-CoV-2 variants and preserving the clinical utility of SA55.

Supplementary Materials: The following supporting information can be downloaded at https://www.mdpi.com/article/10.3390/v18121341/s1, Figure S1: Neutralization activities of KP.3 mutant pseudoviruses by representative RBD-directed monoclonal antibodies. Figure S2: Neutralization activities of KP.3 mutant pseudoviruses by JN.1-convalescent plasma. Figure S3: Soluble ACE2 sensitivity of KP.3 mutant pseudoviruses. Table S1: Information about human donors involved in this study. Table S2: Neutralization activity of SA55 against diverse sarbecoviruses and SARS-CoV-2 variants. Table S3: Raw neutralization phenotypes of KP.3 single-mutant pseudoviruses.

Author Contributions: Conceptualization, Y.C.; methodology, X.N. and F.J.; formal analysis, Y.L. and X.N.; investigation, L.Y., Y.Y., H.S. and J.W.; data curation, Y.L. and X.N.; writing—original draft preparation, Y.L. and Y.C.; writing—review and editing, Y.C.; visualization, Y.L., X.N. and Z.L.; supervision, Y.C.; project administration, F.S.; funding acquisition, Y.C. All authors have read and agreed to the published version of the manuscript.

Funding: This research was funded by Peking University (2025ZD01903803 to F.J.) and Changping Laboratory (2026D-04-01 to Y.C.).

Institutional Review Board Statement: The study was conducted in accordance with the Declaration of Helsinki and approved by the Ethics Committee of Tianjin First Central Hospital (Approval No. 2022N151KY-02; approval date: 4 February 2024).

Informed Consent Statement: Written informed consent has been obtained from the participants to publish this paper.

Data Availability Statement: The neutralization IC_{50} values of SA55 against the tested pseudoviruses are provided in Table S2. The neutralization data for KP.3 mutant pseudoviruses are provided in Table S3. The SA55 DMS escape data generated in this study are available from the corresponding author upon reasonable request. Processed F3 antibody DMS escape scores used for the analysis in Figure 2d were obtained from the dataset accompanying Jian et al. [18], available at Zenodo (https://doi.org/10.5281/zenodo.13893217) [28]. RBD–ACE2 binding affinity DMS data used to color Figure 2c,d were obtained from Taylor and Starr [29,30] and are available at GitHub (https://github.com/tstarrlab/SARS-CoV-2-RBD_DMS_Omicron-XBB-BQ (accessed on 20 October 2026); https://github.com/tstarrlab/SARS-CoV-2-RBD_DMS_Omicron-KP3-LP8 (accessed on 20 October 2026)).

Acknowledgments: We thank all volunteers who provided blood samples. During the preparation of this manuscript, we used ChatGPT (OpenAI; models GPT-5.6 Sol and GPT-6) to assist with language editing and improve the clarity and readability of the manuscript. The authors reviewed and edited the AI-assisted output and take full responsibility for the final content of the manuscript.

Conflicts of Interest: Y.C. is a co-founder of Singlomics Biopharmaceuticals. All other authors declare no conflicts of interest.

References

1. Planas, D.; Saunders, N.; Maes, P.; Guivel-Benhassine, F.; Planchais, C.; Buchrieser, J.; Bolland, W.-H.; Porrot, F.; Staropoli, I.; Lemoine, F.; et al. Considerable escape of SARS-CoV-2 Omicron to antibody neutralization. *Nature* **2022**, *602*, 671–675. [CrossRef] [PubMed]
2. Jian, F.; Yu, Y.; Song, W.; Yisimayi, A.; Yu, L.; Gao, Y.; Zhang, N.; Wang, Y.; Shao, F.; Hao, X.; et al. Further humoral immunity evasion of emerging SARS-CoV-2 BA.4 and BA.5 subvariants. *Lancet Infect. Dis.* **2022**, *22*, 1535–1537. [CrossRef] [PubMed]
3. Planas, D.; Staropoli, I.; Michel, V.; Lemoine, F.; Donati, F.; Prot, M.; Porrot, F.; Guivel-Benhassine, F.; Jeyarajah, B.; Brisebarre, A.; et al. Distinct evolution of SARS-CoV-2 Omicron XBB and BA.2.86/JN.1 lineages combining increased fitness and antibody evasion. *Nat. Commun.* **2024**, *15*, 2254. [CrossRef] [PubMed]
4. Yang, S.; Yu, Y.; Xu, Y.; Jian, F.; Song, W.; Yisimayi, A.; Wang, P.; Wang, J.; Liu, J.; Yu, L.; et al. Fast evolution of SARS-CoV-2 BA.2.86 to JN.1 under heavy immune pressure. *Lancet Infect. Dis.* **2024**, *24*, e70–e72. Correction in *Lancet Infect. Dis.* **2024**, *24*, e56. [CrossRef] [PubMed]
5. Tamura, T.; Ito, J.; Uriu, K.; Zahradnik, J.; Kida, I.; Anraku, Y.; Nasser, H.; Shofa, M.; Oda, Y.; Lytras, S.; et al. Virological characteristics of the SARS-CoV-2 XBB variant derived from recombination of two Omicron subvariants. *Nat. Commun.* **2023**, *14*, 2800. [CrossRef] [PubMed]
6. Ma, K.C.; Castro, J.; Lambrou, A.S.; Rose, E.B.; Cook, P.W.; Batra, D.; Cubenas, C.; Hughes, L.J.; MacCannell, D.R.; Mandal, P.; et al. Genomic Surveillance for SARS-CoV-2 Variants: Circulation of Omicron XBB and JN.1 Lineages—United States, May 2023–September 2024. *MMWR. Morb. Mortal. Wkly. Rep.* **2024**, *73*, 938–945. [CrossRef] [PubMed]
7. Cao, Y.; Wang, J.; Jian, F.; Xiao, T.; Song, W.; Yisimayi, A.; Huang, W.; Li, Q.; Wang, P.; An, R.; et al. Omicron escapes the majority of existing SARS-CoV-2 neutralizing antibodies. *Nature* **2022**, *602*, 657–663. [CrossRef] [PubMed]
8. Iketani, S.; Liu, L.; Guo, Y.; Liu, L.; Chan, J.F.W.; Huang, Y.; Wang, M.; Luo, Y.; Yu, J.; Chu, H.; et al. Antibody evasion properties of SARS-CoV-2 Omicron sublineages. *Nature* **2022**, *604*, 553–556. [CrossRef] [PubMed]
9. Cao, Y.; Yisimayi, A.; Jian, F.; Song, W.; Xiao, T.; Wang, L.; Du, S.; Wang, J.; Li, Q.; Chen, X.; et al. BA.2.12.1, BA.4 and BA.5 escape antibodies elicited by Omicron infection. *Nature* **2022**, *608*, 593–602. [CrossRef] [PubMed]
10. Chen, N.; Decker, K.E.; Schulz, S.R.; Kempf, A.; Nehlmeier, I.; Moldenhauer, A.S.; Dopfer-Jablonka, A.; Behrens, G.M.N.; Stankov, M.V.; Manthey, L.; et al. Comparative Analysis of Host Cell Entry Efficiency and Neutralization Sensitivity of Emerging SARS-CoV-2 Lineages KP.2, KP.2.3, KP.3, and LB.1. *Vaccines* **2024**, *12*, 1236. [CrossRef] [PubMed]
11. Chen, Y.; Zhao, X.; Zhou, H.; Zhu, H.; Jiang, S.; Wang, P. Broadly neutralizing antibodies to SARS-CoV-2 and other human coronaviruses. *Nat. Rev. Immunol.* **2023**, *23*, 189–199. [CrossRef] [PubMed]
12. Tortorici, M.A.; Czudnochowski, N.; Starr, T.N.; Marzi, R.; Walls, A.C.; Zatta, F.; Bowen, J.E.; Jaconi, S.; Di Iulio, J.; Wang, Z.; et al. Broad sarbecovirus neutralization by a human monoclonal antibody. *Nature* **2021**, *597*, 103–108. [CrossRef] [PubMed]
13. Zost, S.J.; Gilchuk, P.; Case, J.B.; Binshtein, E.; Chen, R.E.; Nkolola, J.P.; Schäfer, A.; Reidy, J.X.; Trivette, A.; Nargi, R.S.; et al. Potently neutralizing and protective human antibodies against SARS-CoV-2. *Nature* **2020**, *584*, 443–449. [CrossRef] [PubMed]
14. Cao, Y.; Jian, F.; Zhang, Z.; Yisimayi, A.; Hao, X.; Bao, L.; Yuan, F.; Yu, Y.; Du, S.; Wang, J.; et al. Rational identification of potent and broad sarbecovirus-neutralizing antibody cocktails from SARS convalescents. *Cell Rep.* **2022**, *41*, 111845. [CrossRef] [PubMed]
15. Hu, C.; Zhou, Y.; Meng, X.; Li, J.; Chen, J.; Ying, Z.; Xie, X.S.; Hu, Y.; Cao, Y.; Jin, R. Safety and Intranasal Retention of a Broad-Spectrum Anti-SARS-CoV-2 Monoclonal Antibody SA55 Nasal Spray in Healthy Volunteers: A Phase I Clinical Trial. *Pharmaceutics* **2025**, *17*, 43. [CrossRef] [PubMed]
16. Zhou, Y.; Meng, X.; Li, J.; Zeng, G.; Wang, J.; Cao, Y.; Hu, C.; Jin, R. Safety, tolerability, and pharmacokinetics of anti-SARS-CoV-2 monoclonal antibody SA55 injection in healthy participants. *Antimicrob. Agents Chemother.* **2025**, *69*, e00568-25. [CrossRef] [PubMed]
17. Yisimayi, A.; Song, W.; Wang, J.; Jian, F.; Yu, Y.; Chen, X.; Xu, Y.; Yang, S.; Niu, X.; Xiao, T.; et al. Repeated Omicron exposures override ancestral SARS-CoV-2 immune imprinting. *Nature* **2024**, *625*, 148–156. [CrossRef] [PubMed]
18. Jian, F.; Wang, J.; Yisimayi, A.; Song, W.; Xu, Y.; Chen, X.; Niu, X.; Yang, S.; Yu, Y.; Wang, P.; et al. Evolving antibody response to SARS-CoV-2 antigenic shift from XBB to JN.1. *Nature* **2025**, *637*, 921–929. [CrossRef] [PubMed]
19. Starr, T.N.; Greaney, A.J.; Hilton, S.K.; Ellis, D.; Crawford, K.H.D.; Dingens, A.S.; Navarro, M.J.; Bowen, J.E.; Tortorici, M.A.; Walls, A.C.; et al. Deep Mutational Scanning of SARS-CoV-2 Receptor Binding Domain Reveals Constraints on Folding and ACE2 Binding. *Cell* **2020**, *182*, 1295–1310.e20. [CrossRef] [PubMed]
20. Greaney, A.J.; Loes, A.N.; Crawford, K.H.D.; Starr, T.N.; Malone, K.D.; Chu, H.Y.; Bloom, J.D. Comprehensive mapping of mutations in the SARS-CoV-2 receptor-binding domain that affect recognition by polyclonal human plasma antibodies. *Cell Host Microbe* **2021**, *29*, 463–476.e6. [CrossRef] [PubMed]
21. Dadonaite, B.; Harari, S.; Larsen, B.B.; Kampman, L.; Harteloo, A.; Elias-Warren, A.; Chu, H.Y.; Bloom, J.D. Spike mutations that affect the function and antigenicity of recent KP.3.1.1-like SARS-CoV-2 variants. *J. Virol.* **2025**, *99*, e0142325. [CrossRef] [PubMed]
22. Dadonaite, B.; Brown, J.; McMahon, T.E.; Farrell, A.G.; Figgins, M.D.; Asarnow, D.; Stewart, C.; Lee, J.; Logue, J.; Bedford, T.; et al. Spike deep mutational scanning helps predict success of SARS-CoV-2 clades. *Nature* **2024**, *631*, 617–626. [CrossRef] [PubMed]

23. World Health Organization. *COVID-19 Epidemiological Update–19 January 2024*; World Health Organization: Geneva, Switzerland, 2024.
24. Li, H.; Zhao, C.; Zhang, Y.; Yuan, F.; Zhang, Q.; Shi, X.; Zhang, L.; Qin, C.; Zheng, A. Establishment of replication-competent vesicular stomatitis virus-based recombinant viruses suitable for SARS-CoV-2 entry and neutralization assays. *Emerg. Microbes Infect.* **2020**, *9*, 2269–2277. [CrossRef] [PubMed]
25. Piepenbrink, M.S.; Ma, Y.; Panjwani, S.; Blake, A.R.; Bell, A.M.; Kizziah, J.L.; Mahmoud, S.H.; Ippolito, G.C.; Erdmann, N.B.; Goepfert, P.A.; et al. Emergence of neutralizing RBD antibodies following Omicron infection with limited activity against ancestral SARS-CoV-2. *iScience* **2026**, *29*, 117166. [CrossRef] [PubMed]
26. Greaney, A.J.; Starr, T.N.; Gilchuk, P.; Zost, S.J.; Binshtein, E.; Loes, A.N.; Hilton, S.K.; Huddleston, J.; Eguia, R.; Crawford, K.H.D.; et al. Complete Mapping of Mutations to the SARS-CoV-2 Spike Receptor-Binding Domain that Escape Antibody Recognition. *Cell Host Microbe* **2021**, *29*, 44–57.e9. [CrossRef] [PubMed]
27. Cao, Y.; Jian, F.; Wang, J.; Yu, Y.; Song, W.; Yisimayi, A.; Wang, J.; An, R.; Chen, X.; Zhang, N.; et al. Imprinted SARS-CoV-2 humoral immunity induces convergent Omicron RBD evolution. *Nature* **2023**, *614*, 521–529. [CrossRef] [PubMed]
28. Jian, F.; Cao, Y. *Resources of "Evolving Antibody Response to SARS-CoV-2 Antigenic Shift from XBB to JN.1"*; Zenodo: Geneva, Switzerland, 2024.
29. Taylor, A.L.; Starr, T.N. Deep mutational scans of XBB.1.5 and BQ.1.1 reveal ongoing epistatic drift during SARS-CoV-2 evolution. *PLoS Pathog.* **2023**, *19*, e1011901. [CrossRef] [PubMed]
30. Taylor, A.L.; Starr, T.N. Deep mutational scanning of recent SARS-CoV-2 variants highlights changing amino acid preferences within epistatic hotspot residues. *PLoS Pathog.* **2026**, *22*, e1014074. [CrossRef] [PubMed]
31. Niu, X.; Xiong, D.; He, P.; Yu, L.; Li, Y.; Cai, X.; An, R.; Wang, Y.; Kong, R.; Yu, Y.; et al. Lack of ancestral SARS-CoV-2 imprinting promotes BA.3.2.2 infection in children. *bioRxiv* **2026**. [CrossRef]
32. Yuan, M.; Zhu, X.; He, W.T.; Zhou, P.; Kaku, C.I.; Capozzola, T.; Zhu, C.Y.; Yu, X.; Liu, H.; Yu, W.; et al. A broad and potent neutralization epitope in SARS-related coronaviruses. *Proc. Natl. Acad. Sci. USA* **2022**, *119*, e2205784119. [CrossRef] [PubMed]
33. Yuan, M.; West, B.R.; Foreman, W.B.; Powers, C.; Feng, Z.; Taylor, A.L.; Yu, X.; Wang, G.; Walker, L.; Starr, T.N.; et al. Structural and functional analysis of VYD222: A broadly neutralizing antibody against SARS-CoV-2 variants. *PLoS Pathog.* **2026**, *22*, e1014613. [CrossRef] [PubMed]
34. Rosen, L.E.; Tortorici, M.A.; De Marco, A.; Pinto, D.; Foreman, W.B.; Taylor, A.L.; Park, Y.-J.; Bohan, D.; Rietz, T.; Errico, J.M.; et al. A potent pan-sarbecovirus neutralizing antibody resilient to epitope diversification. *Cell* **2024**, *187*, 7196–7213.e26. [CrossRef] [PubMed]
35. Jian, F.; Wec, A.Z.; Feng, L.; Yu, Y.; Wang, L.; Wang, P.; Yu, L.; Wang, J.; Hou, J.; Berrueta, D.M.; et al. Viral evolution prediction identifies broadly neutralizing antibodies to existing and prospective SARS-CoV-2 variants. *Nat. Microbiol.* **2025**, *10*, 2003–2017. [CrossRef] [PubMed]
36. Arora, P.; Kempf, A.; Nehlmeier, I.; Schulz, S.R.; Jäck, H.M.; Hoffmann, M.; Pöhlmann, S. Entry Efficiency, Protease Dependence, and Antibody-Mediated Neutralization of SARS-CoV-2 Sublineages KP.3.1.1 and XEC. *Vaccines* **2025**, *13*, 385. [CrossRef] [PubMed]
37. Liu, J.; Yu, Y.; Yang, S.; Jian, F.; Song, W.; Yu, L.; Shao, F.; Cao, Y. Virological and antigenic characteristics of SARS-CoV-2 variants LF.7.2.1, NP.1, and LP.8.1. *Lancet Infect. Dis.* **2025**, *25*, e128–e130. [CrossRef] [PubMed]
38. Guo, C.; Yu, Y.; Liu, J.; Jian, F.; Yang, S.; Song, W.; Yu, L.; Shao, F.; Cao, Y. Antigenic and virological characteristics of SARS-CoV-2 variants BA.3.2, XFG, and NB.1.8.1. *Lancet Infect. Dis.* **2025**, *25*, e374–e377. [CrossRef] [PubMed]
39. He, P.; Song, Y.; Guo, C.; Yu, L.; Yu, Y.; Jian, F.; Shao, F.; Cao, Y. Antibody evasion and receptor binding of SARS-CoV-2 variants PQ.16.1.1 and RK.1. *Lancet Infect. Dis.* **2026**, *26*, e386–e387. [CrossRef] [PubMed]
40. Dor, G.; Kekana, D.; Hisner, R.; Martin, D.P.; Korber, B.; Ernst, T.; Levy, A.; Speers, D.; Turville, S.; Sintchenko, V.; et al. Identification and genomic characterization of BA.3.2: A highly divergent BA.3-related SARS-CoV-2 lineage from southern Africa. *Virus Evol.* **2026**, *12*, veag016. [CrossRef] [PubMed]
41. Miyakawa, K.; Sano, K.; Seki, Y.; Sato, R.; Yoshihara, Y.; Mizukami, T.; Hasegawa, H. Cross-neutralization of SARS-CoV-2 BA.3.2.2 lineage by JN.1 mRNA vaccine-induced immunity. *Int. J. Infect. Dis.* **2026**, *170*, 108954. [CrossRef] [PubMed]
42. Kaku, C.I.; Starr, T.N.; Zhou, P.; Dugan, H.L.; Khalifé, P.; Song, G.; Champney, E.R.; Mielcarz, D.W.; Geoghegan, J.C.; Burton, D.R.; et al. Evolution of antibody immunity following Omicron BA.1 breakthrough infection. *Nat. Commun.* **2023**, *14*, 2751. [CrossRef] [PubMed]
43. Jian, F.; Feng, L.; Yang, S.; Yu, Y.; Wang, L.; Song, W.; Yisimayi, A.; Chen, X.; Xu, Y.; Wang, P.; et al. Convergent evolution of SARS-CoV-2 XBB lineages on receptor-binding domain 455–456 synergistically enhances antibody evasion and ACE2 binding. *PLoS Pathog.* **2023**, *19*, e1011868. [CrossRef] [PubMed]
44. Feng, L.; Sun, Z.; Zhang, Y.; Jian, F.; Yang, S.; Xia, K.; Yu, L.; Wang, J.; Shao, F.; Wang, X.; et al. Structural and molecular basis of the epistasis effect in enhanced affinity between SARS-CoV-2 KP.3 and ACE2. *Cell Discov.* **2024**, *10*, 123. [CrossRef] [PubMed]

45. Cao, Y.; Hao, X.; Wang, X.; Wu, Q.; Song, R.; Zhao, D.; Song, W.; Wang, Y.; Yisimayi, A.; Wang, W.; et al. Humoral immunogenicity and reactogenicity of CoronaVac or ZF2001 booster after two doses of inactivated vaccine. *Cell Res.* **2022**, *32*, 107–109. [CrossRef] [PubMed]
46. Cheng, S.M.S.; Mok, C.K.P.; Leung, Y.W.Y.; Ng, S.S.; Chan, K.C.K.; Ko, F.W.; Chen, C.; Yiu, K.; Lam, B.H.S.; Lau, E.H.Y.; et al. Neutralizing antibodies against the SARS-CoV-2 Omicron variant BA.1 following homologous and heterologous CoronaVac or BNT162b2 vaccination. *Nat. Med.* **2022**, *28*, 486–489. [CrossRef] [PubMed]
47. Marcotte, H.; Cao, Y.; Zuo, F.; Simonelli, L.; Sammartino, J.C.; Pedotti, M.; Sun, R.; Cassaniti, I.; Hagbom, M.; Piralla, A.; et al. Conversion of monoclonal IgG to dimeric and secretory IgA restores neutralizing ability and prevents infection of Omicron lineages. *Proc. Natl. Acad. Sci. USA* **2024**, *121*, e2315354120. [CrossRef] [PubMed]
48. Zuo, F.; Cao, Y.; Sun, R.; Wang, Q.; Simonelli, L.; Du, L.; Bertoglio, F.; Schubert, M.; Guerra, C.; Cavalli, A.; et al. Ultrapotent IgA dimeric antibodies neutralize emerging Omicron variants. *J. Virol.* **2025**, *99*, e01740-24. [CrossRef] [PubMed]
49. Harris, C.; Kapingidza, A.B.; San, J.E.; Christopher, J.; Gavitt, T.; Rhodes, B.; Janowska, K.; O'Donnell, C.; Lindenberger, J.; Huang, X.; et al. Design of SARS-CoV-2 RBD immunogens to focus immune responses toward conserved coronavirus epitopes. *J. Virol.* **2025**, *99*, e0046525. [CrossRef] [PubMed]
50. Cohen, A.A.; van Doremalen, N.; Greaney, A.J.; Andersen, H.; Sharma, A.; Starr, T.N.; Keeffe, J.R.; Fan, C.; Schulz, J.E.; Gnanapragasam, P.N.P.; et al. Mosaic RBD nanoparticles protect against challenge by diverse sarbecoviruses in animal models. *Science* **2022**, *377*, eabq0839. [CrossRef] [PubMed]
51. Hauser, B.M.; Sangesland, M.; St. Denis, K.J.; Lam, E.C.; Case, J.B.; Windsor, I.W.; Feldman, J.; Caradonna, T.M.; Kannegieter, T.; Diamond, M.S.; et al. Rationally designed immunogens enable immune focusing following SARS-CoV-2 spike imprinting. *Cell Rep.* **2022**, *38*, 110561. [CrossRef] [PubMed]
52. Fan, C.; Cohen, A.A.; Park, M.; Hung, A.F.-H.; Keeffe, J.R.; Gnanapragasam, P.N.P.; Lee, Y.E.; Gao, H.; Kakutani, L.M.; Wu, Z.; et al. Neutralizing monoclonal antibodies elicited by mosaic RBD nanoparticles bind conserved sarbecovirus epitopes. *Immunity* **2022**, *55*, 2419–2435.e10. [CrossRef] [PubMed]
53. Hauser, B.M.; Sangesland, M.; Lam, E.C.; St Denis, K.J.; Sheehan, M.L.; Vu, M.L.; Cheng, A.H.; Sordilla, S.; Lamson, D.T.; Almawi, A.W.; et al. Heterologous Sarbecovirus Receptor Binding Domains as Scaffolds for SARS-CoV-2 Receptor Binding Motif Presentation. *ACS Infect. Dis.* **2024**, *10*, 553–561. [CrossRef] [PubMed]
54. Starr, T.N.; Greaney, A.J.; Hannon, W.W.; Loes, A.N.; Hauser, K.; Dillen, J.R.; Ferri, E.; Farrell, A.G.; Dadonaite, B.; McCallum, M.; et al. Shifting mutational constraints in the SARS-CoV-2 receptor-binding domain during viral evolution. *Science* **2022**, *377*, 420–424. [CrossRef] [PubMed]
55. Henderson, R.; Edwards, R.J.; Mansouri, K.; Janowska, K.; Stalls, V.; Gobeil, S.M.C.; Kopp, M.; Li, D.; Parks, R.; Hsu, A.L.; et al. Controlling the SARS-CoV-2 spike glycoprotein conformation. *Nat. Struct. Mol. Biol.* **2020**, *27*, 925–933. [CrossRef] [PubMed]
56. Zhou, T.; Tsybovsky, Y.; Gorman, J.; Rapp, M.; Cerutti, G.; Chuang, G.Y.; Katsamba, P.S.; Sampson, J.M.; Schön, A.; Bimela, J.; et al. Cryo-EM Structures of SARS-CoV-2 Spike without and with ACE2 Reveal a pH-Dependent Switch to Mediate Endosomal Positioning of Receptor-Binding Domains. *Cell Host Microbe* **2020**, *28*, 867–879.e5. [CrossRef] [PubMed]
57. Schmidt, F.; Weisblum, Y.; Muecksch, F.; Hoffmann, H.-H.; Michailidis, E.; Lorenzi, J.C.C.; Mendoza, P.; Rutkowska, M.; Bednarski, E.; Gaebler, C.; et al. Measuring SARS-CoV-2 neutralizing antibody activity using pseudotyped and chimeric viruses. *J. Exp. Med.* **2020**, *217*, e20201181. [CrossRef] [PubMed]

Disclaimer/Publisher's Note: The statements, opinions and data contained in all publications are solely those of the individual author(s) and contributor(s) and not of MDPI and/or the editor(s). MDPI and/or the editor(s) disclaim responsibility for any injury to people or property resulting from any ideas, methods, instructions or products referred to in the content.